Chinese Chemical Letters 37 (2026) 112029

Contents lists available at ScienceDirect

Chinese Chemical Letters

journal homepage: www.elsevier.com/locate/cclet

Dual-functional solid additives enable morphology and energy loss regulation for high-efficiency and stable organic photovoltaics

Xinhao Zhong[a], Lingling Zhan[a,*], Yaxin Yang[a], Lu Wei[a], Tianyi Chen[b], Rui Sun[c], Jie Min[c], Hongxiang Li[d], Pei Cheng[d], Shouchun Yin[a,*], Hongzheng Chen[b]

[a] Key Laboratory of Organosilicon Chemistry and Materials Technology of Ministry of Education, College of Material, Chemistry and Chemical Engineering, Hangzhou Normal University, Hangzhou 311121, China
[b] State Key Laboratory of Silicon and Advanced Semiconductor Materials, Department of Polymer Science and Engineering, Zhejiang University, Hangzhou 310027, China
[c] The Institute for Advanced Studies, Wuhan University, Wuhan 430072, China
[d] College of Polymer Science and Engineering, National Key Laboratory of Advanced Polymer Materials, Sichuan University, Chengdu 610065, China

ARTICLE INFO

Article history:
Received 8 August 2025
Revised 23 October 2025
Accepted 27 October 2025
Available online 28 October 2025

Keywords:
Solid-additives
Dual-functional
Vertical phase distribution
High efficiencies
Stability

ABSTRACT

Solid additives have emerged as effective tools for morphology regulation in organic photovoltaics (OPVs), yet simultaneous control over donor and acceptor domains remains challenging. Here, we report a dual-functional solid additive, NSA2, designed to optimize vertical phase distribution and suppress energy loss in PM6:Y6 systems. Compared to the control device with a power conversion efficiency (PCE) of 16.28 %, NSA2-incorporated devices achieve a PCE of 18.51 %, and up to 19.31 % using a layer-by-layer structure with co-additive (DIB). Detailed characterization reveals improved π-π stacking, prolonged crystallization, reduced trap-assisted and bimolecular recombination, and enhanced charge transport. Notably, the non-radiative energy loss ($\Delta E3$) is reduced from 0.214 eV to 0.204 eV, contributing to higher open-circuit voltage. The additive also improves device stability and shows broad compatibility, across other acceptor systems (BTP-eC9-based binary device), achieving PCE of 19.68 %. This work demonstrates a general and scalable strategy for designing multifunctional solid additives to boost efficiency and stability in high-performance OPVs.

© 2026 Published by Elsevier B.V. on behalf of Chinese Chemical Society and Institute of Materia Medica, Chinese Academy of Medical Sciences.

Organic photovoltaics (OPVs) are recognized as a compelling candidate for next-generation solar energy technologies due to their advantageous features such as lightweight form factor, mechanical flexibility, cost-effective manufacturing, and compatibility with roll-to-roll processing [1–11]. Recent breakthroughs in material design and device optimization have enabled OPVs to exceed 20 % power conversion efficiency (PCE), establishing a promising route toward practical application [12–19]. Despite this progress, further advancement is hindered by fundamental limitations, especially substantial non-radiative recombination energy loss ($\Delta E_{loss}^{non-rad.}$), which curtail the open-circuit voltage (V_{OC}) and overall device performance [20–26].

Compared to inorganic counterparts, where $\Delta E_{loss}^{non-rad.}$ is typically below 100 mV, OPVs often exhibit $\Delta E_{loss}^{non-rad.}$ values exceeding 200 mV, largely due to imperfect molecular ordering and insufficient control over donor/acceptor (D/A) interfacial interactions [27–30]. Consequently, precise regulation of active layer morphology, especially at the nanoscale, is essential for minimizing $\Delta E_{loss}^{non-rad.}$ and promoting efficient charge separation and transport [31–33]. A widely used approach to morphological tuning involves incorporating high-boiling-point liquid additives (*e.g.*, 1,8-diiodooctane (DIO) or 1-chloronaphthalene (CN)), which slow solvent evaporation and facilitate favorable phase separation. However, residual liquid additives can persist as microscopic droplets within the active layer, negatively affecting film uniformity and device longevity. In recent years, attention has shifted toward using solid-state additives as an alternative, offering greater stability and improved process compatibility [34–37].

Solid additives with well-defined molecular structures enable tuning of intermolecular interactions by modulating parameters such as π-conjugation, steric bulk, and electrostatic potential (ESP). For instance, additives incorporating triphenylamine (TPA) and cyanoarene connected *via* π-bridging units have been shown to promote polymer chain pre-aggregation and enhance domain purity [38]. However, many of these additives feature a positive

* Corresponding authors.
E-mail addresses: linglingzhan@hznu.edu.cn (L. Zhan), yinsc@hznu.edu.cn (S. Yin).

https://doi.org/10.1016/j.cclet.2025.112029
1001-8417/© 2026 Published by Elsevier B.V. on behalf of Chinese Chemical Society and Institute of Materia Medica, Chinese Academy of Medical Sciences.

surface potential, favoring interaction with electron-rich regions but showing limited compatibility with non-fullerene acceptors (NFAs), which are typically more electron-deficient [39–41]. To effectively manipulate the morphology of both donor and acceptor domains, it is imperative to design dual-functional solid additives that offer simultaneous modulation of intermolecular interactions in both phases. Yet, such strategies remain underexplored.

Herein, we report a new family of solid additives (NSA1–3 series) designed to simultaneously address D/A microstructure control. Strategic fluorine incorporation at terminal arenes shifts ESP from positive to negative, enhancing the compatibility with NFAs, while alkyl chain engineering on π-bridges modulates conformational flexibility and steric hindrance [42–45]. Furthermore, structural variation on the TPA terminal allowed adjustment of molecular planarity. Among the series, NSA2, with a linear alkyl chain and a TPA segment, exhibited the lowest ESP and smallest torsional angle, thus reducing its steric hindrance, and achieving higher degrees of freedom as the additive. In the PM6:Y6 binary system, NSA2 was found to facilitate donor pre-aggregation and regulate the phase distribution of acceptor domains. This led to a well-defined vertical phase-separated morphology, enhanced exciton dissociation, and balanced carrier mobilities. More notably, NSA2 demonstrated selective surface enrichment in the donor layer during layer-by-layer (LBL) deposition, enabling cooperative optimization of both donor and acceptor stacking. As a result, LBL devices incorporating NSA2 achieved a high PCE of 19.68 %, among the top reported efficiencies for NFA-based binary systems, alongside a reduced energy loss. Through concurrent ESP tuning and conformational control, this approach offers a promising route for advancing the efficiency, stability, and scalability of high-performance OPVs.

Fig. 1a displays the chemical structures of the donor polymer PM6, the NFA Y6, and the newly developed solid additives TPA-BO–NF (NSA1), TPA-TA-NF (NSA2), and TPE-TA-NF (NSA3). Synthetic routes of NSA1–3 are outlined in Fig. S1 (Supporting information), and their molecular structures were verified by ^{1}H nuclear magnetic resonance (NMR) spectra (Figs. S2–S4 in Supporting information) and matrix-assisted laser desorption/ionization time of flight (MALDI-TOF) mass spectra (Fig. S5 in Supporting information). Cyclic voltammetry (CV) profiles and corresponding energy level diagrams are shown in Fig. S6 (Supporting information). The normalized ultraviolet visible (UV–vis) absorption spectra, alongside the normalized photoluminescence (PL) spectra of PM6, Y6, and NSA1–3 films as presented in Fig. 1b. Notably, the emission bands of NSA1–3 partially overlap with the absorption profile of Y6, suggesting the potential for Förster resonance energy transfer (FRET), which may enhance light-harvesting and spectral utilization [46–48]. To elucidate charge redistribution, density functional theory (DFT) calculations mapped the ESP of each additive (Fig. 1c). Terminal fluorine atoms impart strong electron-withdrawing character, resulting in uniformly negative ESP values for NSA1–3 that favor interactions with electron-deficient acceptors such as Y6 [49]. Fig. 1d illustrates how side-chain engineering on the thiophene π-bridge modulates molecular conformation. The linear alkyl chain in NSA2 flatten the molecular backbone compared to NSA1, lowering the TPA-core torsion angle from 33.92° to 31.49° and the TPA-naphthalene dihedral angle from 75.20° to 39.48°. Replacing TPA with tetraphenylethylene (TPE) in NSA3 further reduces the terminal dihedral angle to 27.93°, indicating diminished steric hindrance at the junction. However, this modification increases internal TPE moiety torsion to 53.18°, revealing a trade-off between molecular flexibility and intramolecular rigidity. Additives with smaller dihedral angles experience reduced steric congestion and improved conformational adaptability, thereby facilitating more effective morphological regulation in the active layer.

To evaluate the compatibility and phase distribution of active-layer components, contact angle measurements and parameter calculations were performed (Fig. S7 and Table S1 in Supporting information). Material miscibility was assessed *via* the Flory-Huggins interaction parameter (χ), with lower values indicating better compatibility. NSA1 and NSA2 showed stronger affinity for Y6, while NSA3 favored PM6 [50]. All three additives improved PM6:Y6 miscibility, potentially enabling finer phase separation. The χ values for NSA1–3 blends were 0.0818, 0.5876, and 0.0695, respectively, all lower than that of pristine PM6:Y6 ($\chi = 0.7708$). However, the very low χ values for NSA1 and NSA3 may lead to over-mixing, potentially impeding charge transport. Surface energy (γ) analysis revealed that NSA1–3 have higher γ than PM6. Consequently, these additives are expected to migrate towards the film surface in PM6 blends to minimize total surface energy. In bulk heterojunction (BHJ) films, this can promote vertical phase separation, with enhanced acceptor concentration near the cathode, promoting electron extraction.

Vertical composition critically affects exciton generation, charge transport, and collection [51]. Film depth-dependent absorption spectroscopy (FLAS) was used to assess exciton generation profiles (Fig. 1e). Compared to the control, NSA1–3-containing films exhibited stronger absorption across the depth, indicating higher exciton generation and enhanced photocurrent potential. FLAS-derived component profiles (Fig. 1f) showed that, unlike the uniform D:A distribution in the control, NSA1–3 blends formed vertically stratified morphologies with acceptor enrichment at the cathode. NSA2 yielded the most favorable vertical structure, with minimal acceptor at the anode, while NSA1 and NSA3 showed excess acceptor at both interfaces, consistent with contact angle results. Similar vertical optimization was observed when NSA2 was combined with 3,5-dichlorobromobenzene (DCBB) (Fig. S8 in Supporting information). PM6 and Y6 showed consistent absorption across film depths (Fig. S9 in Supporting information), indicating uniform energy levels and low trap density. Transfer matrix simulations (Figs. S10 and S11 in Supporting information) confirmed enhanced exciton generation in all NSA1–3 systems, with maxima shifting toward the cathode, thereby balancing charge mobilities. These results confirm that solid additives optimize vertical phase distribution, with NSA2 offering the most desirable vertical structure and superior potential as efficient additive.

To evaluate the effect of solid additives, OPV devices were fabricated using a conventional structure of ITO/HTL/active layer/ETL/Ag. Optimized processing conditions and photovoltaic parameters are listed in Table S2 (Supporting information), with corresponding *J-V* and EQE curves shown in Fig. S12 (Supporting information). Optimized *J-V* curves are presented in Fig. 2a, and key parameters are summarized in Table 1. The control PM6:Y6 device exhibited a V_{OC} of 0.851 V, short-circuit current density (J_{SC}) of 27.08 mA/cm^2, fill factor (FF) of 70.63 %, and PCE of 16.28 %, consistent with reported ones. Incorporation of NSA1–3 led to simultaneous improvements in all three parameters, with NSA2 yielding the most significant enhancement. Co-addition of NSA2 and DCBB further increased the PCE to 18.51 %. Considering the spontaneous surface migration of solid additives in the donor phase, a LBL strategy was adopted: NSA2 was introduced into the PM6 layer and DCBB or 1,4-diiodobenzene (DIB) into Y6, leveraging vertical phase distribution control from both additives [52–54]. With 2PACz as the HTL, the resulting LBL device achieved a PCE of 19.31 %, among the highest reported for Y6-based binary OPVs [55]. EQE spectra of all devices (Fig. 2b) confirmed high reproducibility, with integrated J_{SC} deviations below 4.5 %. NSA1–3 are non-volatile solid additives that persist in the active layer after thermal-annealing at the optimal temperature of 80 °C (Fig. S13 in Supporting information), markedly reducing batch-to-batch variability and enhancing reproducibility, benefits shared with other non-volatile additives previously reported [56–58]. Furthermore, FLAS analysis of LBL active layers revealed more pronounced vertical stratification under the

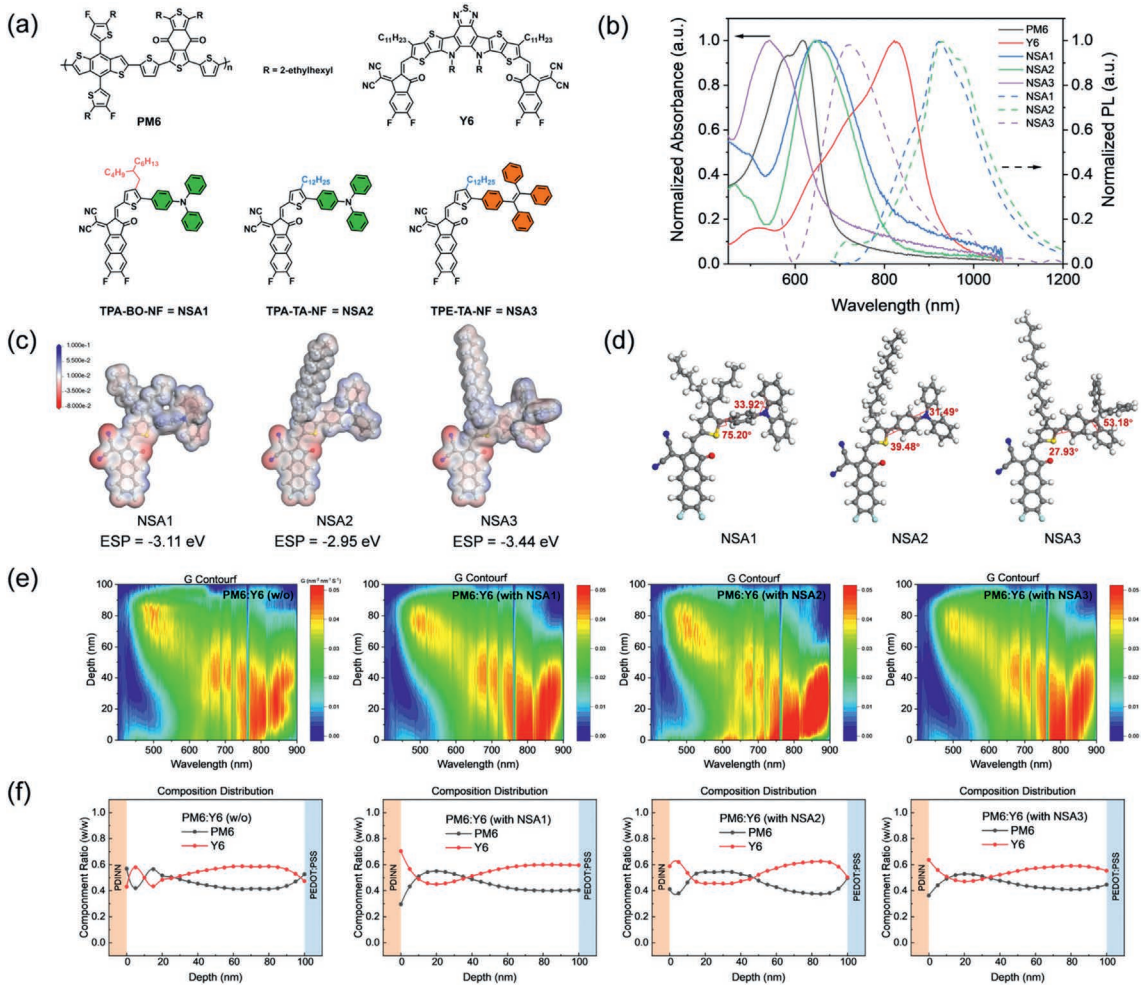


Fig. 1. (a) Chemical structures of PM6, Y6, NSA1, NSA2, and NSA3. (b) Normalized absorption spectra of PM6, Y6, NSA1, NSA2, NSA3 films, and Normalized PL spectra of NSA1, NSA2, NSA3 films. (c) Electrostatic potential distributions, and (d) optimized geometries and dihedral angles of relevant molecules. (e) Film-depth-dependent light absorption spectroscopy (FLAS) of PM6:Y6 (w/o), PM6:Y6 (with NSA1), PM6:Y6 (with NSA2) and PM6:Y6 (with NSA3) films. (f) Relative weight ratio of D:A as a function of position in films obtained from FLAS.

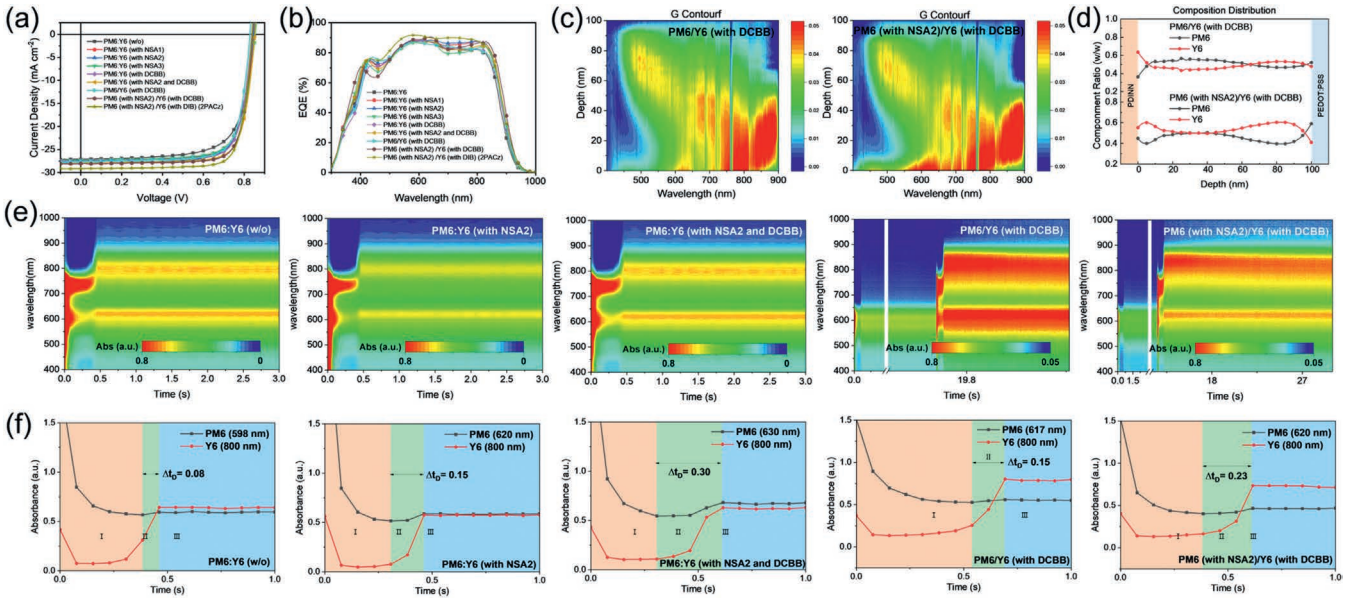


Fig. 2. (a) *J-V* curves of binary devices with various additives. (b) EQE curves of the relevant devices. (c) FLAS of PM6/Y6 (with DCBB) and PM6 (with NSA2)/Y6 (with DCBB) films. (d) Relative weight ratio of D:A as a function of position in films obtained from FLAS. (e) Time-dependent contour maps of *in situ* UV–vis absorption spectra of three BHJ-type films (PM6:Y6 (w/o), PM6:Y6 (with NSA2), PM6:Y6 (with NSA2 and DCBB)) and two LBL-type films (PM6/Y6 (with DCBB), PM6 (with NSA2)/Y6 (with DCBB) during spin coating). (f) Time evolution of peak location and normalized intensity of donor and acceptor.

Table 1
Photovoltaic parameters of devices with different additives and structures.

Active layer	V_{OC} (V)	J_{SC} (mA/cm^2)	J_{cal} [a] (mA/cm^2)	FF (%)	PCE [b] (%)
PM6:Y6 (w/o)	0.851 (0.852 ± 0.003)	27.08 (26.87 ± 0.35)	26.08	70.63 (70.16 ± 0.49)	16.28 (16.05 ± 0.16)
PM6:Y6 (with NSA1)	0.847 (0.849 ± 0.003)	27.54 (27.31 ± 0.13)	26.96	74.18 (74.00 ± 0.25)	17.29 (17.14 ± 0.09)
PM6:Y6 (with NSA2)	0.845 (0.847 ± 0.002)	27.95 (27.81 ± 0.24)	27.07	74.64 (74.61 ± 0.37)	17.64 (17.57 ± 0.08)
PM6:Y6 (with NSA3)	0.854 (0.854 ± 0.002)	27.29 (26.91 ± 0.36)	26.18	74.09 (74.72 ± 0.57)	17.27 (17.18 ± 0.11)
PM6:Y6 (with DCBB)	0.837 (0.839 ± 0.003)	27.50 (27.18 ± 0.32)	26.31	77.57 (77.59 ± 0.35)	17.86 (17.70 ± 0.16)
PM6:Y6 (with NSA2 and DCBB)	0.851 (0.848 ± 0.003)	27.96 (27.57 ± 0.20)	26.72	77.78 (78.30 ± 0.42)	18.51 (18.31 ± 0.11)
PM6/Y6 (with DCBB)	0.829 (0.826 ± 0.003)	27.65 (27.47 ± 0.17)	26.49	76.32 (76.45 ± 0.43)	17.48 (17.34 ± 0.15)
PM6 (with NSA2)/Y6 (with DCBB)	0.841 (0.840 ± 0.003)	28.02 (27.94 ± 0.30)	27.20	78.98 (78.61 ± 0.21)	18.63 (18.44 ± 0.10)
PM6 (with NSA2)/Y6 (with DIB) [c]	0.839 (0.836 ± 0.002)	29.15 (28.98 ± 0.23)	28.01	79.18 (79.14 ± 0.37)	19.31 (19.11 ± 0.12)

[a] Integrated current densities from EQE curves.
[b] Average PCEs from 10 devices.
[c] The HTL is 2PACz.

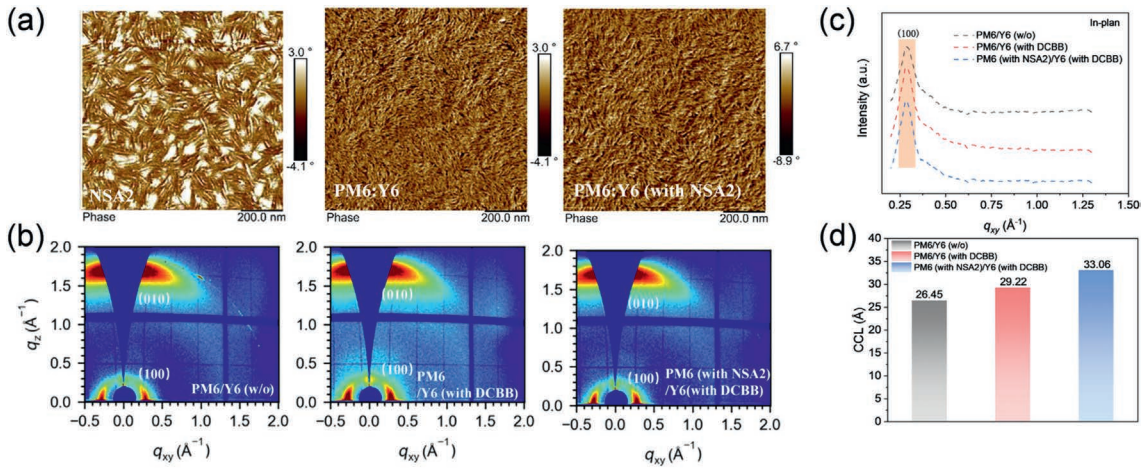


Fig. 3. (a) AFM phase images of NSA2 neat film, PM6:Y6 (w/o) and PM6:Y6 (with NSA2) blend films. (b) 2D GIWAXS images of PM6/Y6 (w/o), PM6/Y6 (with DCBB), and PM6 (with NSA2)/Y6 (with DCBB) LBL-type films. (c) 1D intensity profiles of relevant films along in-plane directions. (d) CCL values of various films.

influence of NSA2, with acceptor enrichment near the cathode and donor accumulation toward the anode, promoting efficient carrier transport and collection.

To study the film formation and phase evolution dynamics, *in situ* UV–vis absorption spectroscopy was performed (Fig. 2e), enabling real-time analysis of film-forming behavior. The film formation process can be divided into three stages: (I) solvent evaporation, (II) nucleation and crystal growth, and (III) film completion. The corresponding phase evolution extracted from *in-situ* spectra is shown in Fig. 2f. In the pristine PM6:Y6 blend, donor crystallization initiates at $t = 0.38$–0.46 s, with a nucleation duration (Δt_D) of 0.08 s. Upon introducing NSA2, the donor nucleation starts earlier, at $t = 0.31$–0.46 s, and Δt_D extends to 0.15 s, indicating enhanced molecular pre-aggregation. This prolonged crystallization window promotes more ordered molecular packing and higher crystallinity, facilitating stronger π-π stacking, consistent with subsequent morphology results. A similar trend is observed in LBL-processed devices, where NSA2 incorporation delays film completion and regulates crystallization kinetics. In contrast, the unmodified PM6:Y6 film undergoes faster crystallization within a shorter time window, leading to rougher morphology and less controlled phase separation. Overall, the introduction of solid additives slowed down the crystallization process, enabling finer phase separation and improved molecular ordering. This regulated film formation is favorable for optimizing exciton dynamics and charge transport, ultimately contributing to enhanced device performance.

To investigate the surface morphology of the active layer, atomic force microscopy (AFM) was performed. As shown in Fig. 3a and Fig. S14 (Supporting information), the root-mean-square (RMS) roughness decreased from 1.18 nm in the additive-free film to 1.14 nm upon addition of NSA2, indicating a more favorable phase separation scale and a well-interconnected fibrous network. The molecular packing and crystallinity within the films were further examined using grazing-incidence wide-angle X-ray scattering (GIWAXS), based on a LBL device configuration. Figs. 3b and c and Fig. S15 (Supporting information) show the 2D GIWAXS patterns and corresponding 1D line-cut profiles. All three blend films exhibited distinct (100) diffraction peaks in both in-plane (IP) and out-of-plane (OOP) directions, along with a prominent (010) π-π stacking peak in the OOP direction, suggesting a mixed face-on and edge-on orientation, with face-on as the dominant texture. In the unmodified film, the (100) diffraction peak appeared at $q = 0.289$ Å^{-1} in the IP direction. Upon DCBB optimization, this peak shifted to $q = 0.286$ Å^{-1}, indicating an increased lamellar spacing and enhanced peak intensity. With the additional incorporation of NSA2 into the donor layer, the lamellar peak further shifted to $q = 0.283$ Å^{-1} with increased intensity, demonstrating improved molecular packing and crystallinity driven by the dual solid-additive strategy. In the OOP direction, a pronounced (010) π-π stacking peak appeared at $q \approx 1.70$ Å^{-1} for the pristine film, with a full width at half maximum (FWHM) of 0.238 Å^{-1}, corresponding to a crystal coherence length (CCL) of 26.46 Å (Fig. 3d, Table S3 in Supporting information). Upon additive optimization, the FWHM narrowed to 0.19 Å^{-1}, and the CCL increased to 33.06 Å, indicating tighter π-π stacking and more ordered molecular orientation, favorable for charge transport. The refined phase separation and enhanced molecular ordering in NSA2-optimized films account for the observed improvements in J_{SC} and FF, contributing to the improved device performance.

Charge recombination behavior was evaluated by analyzing the dependence of V_{OC} and J_{SC} on light intensity. As shown in Fig. S16 (Supporting information), the slope n from the linear relationship of $V_{OC} \propto n(kT/q)\ \ln P_{light}$ reflects trap-assisted recombination (Fig. S16a). The pristine film showed $n = 1.72$, while all additive-optimized systems exhibited reduced n values. Notably, NSA2 yielded the lowest value ($n = 1.32$), indicating more effective suppression of trap-assisted recombination compared to the reported DCBB system. The relationship between J_{SC} and P_{light} follows $J_{SC} \propto P_{light}{}^{\alpha}$, where α indicates the extent of bimolecular recombination. As shown in Fig. S16b, all systems exhibited α values close to 1, suggesting minimal bimolecular recombination. The slightly lower recombination in the pristine film is attributed to its larger phase separation, consistent with contact angle and AFM results. This reduced recombination is one factor contributing to the higher FF observed in optimized devices.

Charge carrier mobilities were further assessed by measuring space-charge-limited current (SCLC) in hole-only and electron-only devices (Figs. S16c and S17, Table S4 in Supporting information). Compared to the control, all additive-optimized systems showed enhanced and more balanced charge mobilities. Hole mobilities increased to 1.95, 2.75, and 3.65×10^{-4} $cm^2\ V^{-1}\ s^{-1}$, while corresponding electron mobilities reached 1.39, 2.09, and 3.23×10^{-4} $cm^2\ V^{-1}\ s^{-1}$. These improvements stem from more favorable vertical phase distribution and reduced trap-assisted and bimolecular recombination during transport. Together, these factors contribute to the higher J_{SC} and FF observed in NSA2-optimized devices.

For systems with identical bandgaps (Fig. S18 in Supporting information), the dual-additive device exhibited a significantly higher V_{OC} than the DCBB-only optimized counterpart, indicating reduced E_{loss}. To quantify this, E_{loss} was analyzed using electroluminescence (EL) and Fourier-transform photocurrent spectroscopy (FTPS)-EQE measurements (Figs. S16d and e), with detailed values summarized in Table S5 (Supporting information). Notably, the introduction of NSA2 reduced the total E_{loss} from 0.573 eV to 0.559 eV, primarily due to a decrease in ΔE_3 from 0.214 eV to 0.204 eV. As ΔE_3 is directly linked to $\Delta E_{loss}^{non-rad.}$, the external electroluminescence quantum efficiency (EQE-EL) was measured. The results showed a significant increase in EL efficiency (Fig. S16f), leading to a reduction in $\Delta E_{loss}^{non-rad.}$ from 0.216 eV to 0.206 eV in the NSA2-optimized device, resulting in enhanced V_{OC}.

A key advantage of solid additives lies in their ability to enhance long-term device stability. To compare this effect, maximum power point (MPP) tracking tests under continuous illumination were conducted on devices optimized with a liquid additive (CN), a commercial solid additive (DCBB), and our NSA2. As shown in Fig. S19 (Supporting information), devices incorporating our solid additive NSA2 exhibited the highest operational stability. Storage stability tests in a nitrogen atmosphere further confirmed its superior performance (Fig. S16g). After 1066 h of storage, devices with CN retained 82 % of their initial PCE, while those containing DCBB and NSA2 preserved 86 % and 90 %, respectively. To assess the generality of our additive design strategy, NSA2 was incorporated into two representative binary systems, PM6:L8-BO and BTP-eC9. In both cases, NSA2-optimized devices achieved high photovoltaic performance, with PCEs 19.55 % and 19.68 %. Corresponding *J-V* and EQE curves are shown in Figs. S16h and i, and detailed device parameters are listed in Table S6 (Supporting information). The impressive photovoltaic performance achieved through our solid additive design highlights the feasibility and scalability of the proposed strategy.

In summary, we developed a series of structurally tunable solid additives (NSA1–3), with NSA2 demonstrating outstanding capability in simultaneously optimizing both donor and acceptor morphology in PM6:NFA-based OPVs. Through rational molecular design, modulating electrostatic potential, molecular conformation, and steric characteristics, NSA2 enabled precise control over vertical phase distribution, crystallinity, and energy loss pathways. Comprehensive characterization revealed that NSA2 promotes donor pre-aggregation, enhances π-π stacking, and improves exciton generation and charge transport. Devices incorporating NSA2 achieved a high PCE of 18.51 %, which further increased to 19.31 % in a LBL architecture using DIB as a co-additive in Y6-based binary OPVs. Moreover, the proposed solid additive design strategy not only offers a practical route to reduce E_{loss} and boost efficiency, but also exhibits strong universality across different material systems (achieved a high PCE of 19.68 % in BTP-eC9-based binary device). This work provides valuable insights for designing next-generation solid-state additives toward scalable, efficient, and durable OPVs.

CRediT authorship contribution statement

Xinhao Zhong: Writing – original draft, Validation, Resources, Methodology, Investigation, Formal analysis, Data curation. **Lingling Zhan:** Writing – review & editing, Visualization, Supervision, Project administration, Investigation, Funding acquisition, Conceptualization. **Yaxin Yang:** Methodology, Investigation. **Lu Wei:** Software, Resources. **Tianyi Chen:** Validation, Software, Resources. **Rui Sun:** Investigation. **Jie Min:** Validation. **Hongxiang Li:** Software. **Pei Cheng:** Software, Resources. **Shouchun Yin:** Writing – review & editing, Funding acquisition. **Hongzheng Chen:** Writing – review & editing, Visualization, Resources, Project administration.

Declaration of competing interest

The authors declare that they have no known competing financial interests or personal relationships that could have appeared to influence the work reported in this paper.

Acknowledgments

This work is supported by Natural Science Foundation of Zhejiang Province (Nos. LQ23E030002, LZ23B040001), the National Natural Science Foundation of China (Nos. 52303226, 21971049, 52472256). A portion of this work is based on the data obtained at Beijing Synchrotron Radiation Facility (BSRF) and Shanghai Synchrotron Radiation Facility (SSRF). The authors gratefully acknowledge the cooperation of the beamline scientists at BSRF-1W1A, SRRF-BL16B1 and SRRF-BL02U2.

Supplementary materials

Supplementary material associated with this article can be found, in the online version, at doi:10.1016/j.cclet.2025.112029.

References

[1] Z. Wang, D. Zhang, L. Yang, et al., Science 387 (2025) 381–387.
[2] N. Yang, S. Zhang, Y. Cui, et al., Nat. Rev. Mater. 10 (2025) 404–424.
[3] H. Zhang, Y. Liu, G. Ran, et al., Adv. Mater. 36 (2024) 2400521.
[4] R. Sun, X. Yuan, X. Yang, et al., Joule 8 (2024) 2523–2538.
[5] J. Ding, H. Mou, H. Chen, et al., Adv. Mater. 37 (2025) 2420439.
[6] J. Yu, L. Hao, K. Zhang, et al., Chem. Eng. J. 500 (2024) 156887.
[7] E.Y. Shin, J. Park, D.J. Kim, et al., Chem. Eng. J. 499 (2024) 156116.
[8] X. Liu, S. Xu, B. Tang, X. Song, Chem. Eng. J. 497 (2024) 154944.
[9] W. Gao, R. Ma, T.A. Dela Peña, et al., Nat. Commun. 15 (2024) 1946.
[10] Q. Bei, B. Zhang, K. Wang, et al., Chin. Chem. Lett. 35 (2024) 108438.
[11] Z. Zhang, Y. Chen, Y. Zhang, C. Zhan, Chin. Chem. Lett. 36 (2025) 110083.
[12] R. Ma, Z. Luo, Y. Zhang, et al., Sci. China Mater. 68 (2025) 1689–1701.
[13] L. Wang, C. Chen, Z. Gan, et al., Adv. Mater. 37 (2025) 2419923.
[14] H. Ren, J. Chen, Y. Zhang, et al., Sci. Adv. 10 (2024) eadp9439.
[15] J. Wang, P. Wang, T. Chen, et al., Angew. Chem. Int. Ed. 64 (2025) e202423562.
[16] X. Song, B. Zhang, X. Liu, et al., Adv. Mater. 37 (2025) 2418393.
[17] Y. Yu, J. Wang, Z. Chen, et al., Sci. China Chem. 67 (2024) 4194–4201.
[18] X. Wang, Q. Liang, A. Zhang, et al., J. Am. Chem. Soc. 147 (2025) 9261–9272.
[19] L. Zhu, M. Zhang, G. Zhou, et al., Joule 8 (2024) 3153–3168.

[20] S. Yang, Z. Chen, J. Zhu, et al., Adv. Mater. 36 (2024) 2401789.
[21] L. Zhang, D. Deng, K. Lu, Z. Wei, Adv. Mater. 36 (2024) 2302915.
[22] H. Wu, H. Lu, Y. Li, et al., Nat. Commun. 15 (2024) 2693.
[23] Y. Jiang, K. Liu, F. Liu, et al., Adv. Mater. 37 (2025) 2500282.
[24] X. Kong, L. Zhan, Z. Li, et al., Aggregate 5 (2024) e5535.
[25] P. Zhang, Z. Zhang, H. Sun, et al., Chin. Chem. Lett. 35 (2024) 108802.
[26] L. Zhan, S. Li, Y. Li, et al., Joule 6 (2022) 662–675.
[27] R. Wang, L. Han, N. Li, et al., Adv. Energy Mater. 14 (2024) 2400609.
[28] T.A.P. Dela Peña, R. Ma, Z. Xing, et al., Energy Environ. Sci. 16 (2023) 3416–3429.
[29] C. Li, G. Yao, X. Gu, et al., Nat. Commun. 15 (2024) 8872.
[30] D. Luo, R. Su, W. Zhang, Q. Gong, R. Zhu, Nat. Rev. Mater. 5 (2020) 44–60.
[31] S. Ullbrich, J. Benduhn, X. Jia, et al., Nat. Mater. 18 (2019) 459–464.
[32] D. Qian, Z. Zheng, H. Yao, et al., Nat. Mater. 17 (2018) 703–709.
[33] S. Liu, J. Yuan, W. Deng, et al., Nat. Photonics 14 (2020) 300–305.
[34] W.A. Memon, Z. Deng, F. He, EnergyChem 6 (2024) 100129.
[35] Z. Li, X. Kong, Y. Liu, et al., Chin. Chem. Lett. 35 (2024) 109378.
[36] D. Hu, H. Tang, C. Chen, et al., Adv. Mater. 36 (2024) 2406949.
[37] P. Guo, Y. Tao, J. Liang, et al., Chem. Eng. J. 512 (2025) 162339.
[38] Z. Li, L. Zhan, H. Qiu, et al., Energy Environ. Sci. 17 (2024) 17.
[39] R. Yu, R. Shi, Z. He, et al., Angew. Chem. Int. Ed. 62 (2023) e202308367.
[40] R. Yu, H. Yao, L. Hong, et al., Nat. Commun. 9 (2018) 4645.
[41] H. Lu, K. Chen, R.S. Bobba, et al., Adv. Mater. 34 (2022) 2205926.
[42] W. Lai, S. Karuthedath, C. Xiao, et al., Chin. Chem. Lett. 35 (2024) 108287.
[43] W. Ma, X. He, T. Chen, et al., Chin. Chem. Lett. 35 (2024) 109099.
[44] Y. Gao, H. Zhang, Y. Xie, et al., Chin. Chem. Lett. 37 (2026) 111622.
[45] J. Zhu, A. Tang, L. Tang, et al., Chin. Chem. Lett. 36 (2025) 110233.
[46] H. Jin, N. Mallo, G. Zhang, et al., Adv. Funct. Mater. 35 (2025) 2420416.
[47] L. Zhan, S. Li, H. Zhang, et al., Adv. Sci. 5 (2018) 1800755.
[48] W. Chen, H. Jiang, G. Huang, et al., Solar RRL 2 (2018) 1800101.
[49] L. Ma, H. Yao, J. Wang, et al., Angew. Chem. Int. Ed. 60 (2021) 15988–15994.
[50] L. Ye, H. Hu, M. Ghasemi, et al., Nat. Mater. 17 (2018) 253–260.
[51] X. Kong, L. Zhan, S. Li, et al., Chem. Eng. J. 473 (2023) 145201.
[52] J. Wang, Y. Wang, P. Bi, et al., Adv. Mater. 35 (2023) 2301583.
[53] L. Zhan, S. Li, X. Xia, et al., Adv. Mater. 33 (2021) 2007231.
[54] Y. Liu, L. Zhan, Z. Li, et al., Adv. Sci. 11 (2024) 2405303.
[55] C. Li, J. Song, H. Lai, et al., Nat. Mater. 24 (2025) 433–443.
[56] L. Liu, Y. Kan, K. Gao, et al., Adv. Mater. 32 (2020) 1907604.
[57] W. Wu, Y. Luo, T.A. Dela Peña, et al., Adv. Energy Mater. 14 (2024) 2400354.
[58] Y.T. Wang, W.J. Sun, Y. Zhang, et al., Angew. Chem. Int. Ed. 64 (2024) e202417643.